INTERNATIONAL JOURNAL OF
NUMERICAL ANALYSIS AND MODELING
Volume 4, Number 3-4, Pages 671–689

MODELING AND COMPUTATION OF PULSED LASER MATERIALS PROCESSING

THOMAS P. SVOBODNY

This paper is dedicated to Max Gunzburger

Abstract. Pulsed laser materials processing incorporates many physical processes, the modeling of which requires disparate techniques. We focus on two closely related topics that arise in laser processing. First, we illustrate by use of numerical simulation the distinction between metals and ceramics in their response to laser fluence. Second we explain recent experiments that indicate that the substrate heater is a strong control parameter in laser processing, and this can be understood from the point of view of shock dynamics.

Key Words. Laser ablation, melting, nonlinear heat conduction, plume dynamics, plume shape, emission spectroscopy, shock, substrate heating, temperature gradient, time-of-flight, vorticity, phase transition, heat conduction, radiation, thermophysical modeling

1. Introduction

Lasers have a wide range of uses in materials processing. Besides the surface ablation of material and structural destruction of high-power lasers, lasers can be used at lower energy settings for annealing, machining, welding, hardening, glazing, as well as promoting of chemical reactions on the surface and in the bulk ([1], [2]). An example of the wide range of laser usage in processing is given by the deposition of films of high temperature superconductors; lasers are used not only in the ablation-deposition process, but in treatment and deposition of metallic and ceramic substrate elements and in post-deposition treatment. Practically all materials can be treated using lasers. However the setting of power parameters is a function of the energy absorbed in the light/material interaction and the thermal properties of the specific material. Thus, there may be a difference of several orders of magnitude of the power settings to accomplish a particular task for different materials. And of course, different lasers will be better matches than others for a particular task on a given material. The actual light energy available to a workpiece depends on the laser power, frequency, optical train, and ambient atmosphere. The energy absorbed depends on the optical properties of the material, the surface finish, and temperature and phase of the material. This energy is converted into heat available for conduction, radiation, and the latent heat of melting and vaporization. When the laser intensity is high enough, material will be ablated from the surface. The ablation process involves supercritical phase transitions, material strength, shocks, and plasma formation. The resulting plume can then be used for deposition on a substrate. Laser deposition is currently the subject of much

2000 *Mathematics Subject Classification.* 76L05, 74N20.

This research was supported by AFOSR under contract F49620-02-1-0261, and a computing grant from Ohio Supercomputer Center.

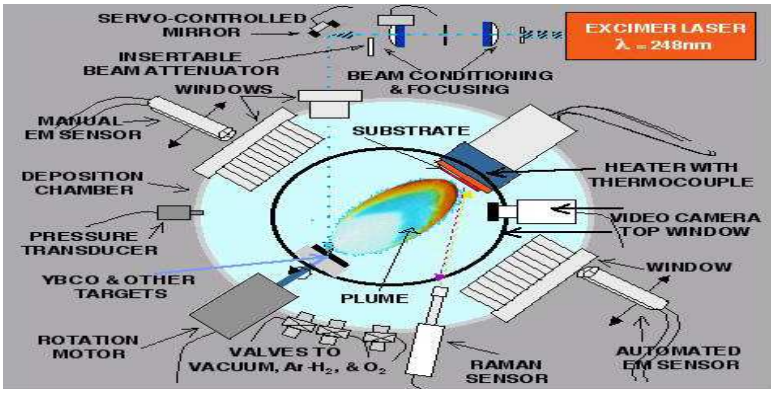

FIGURE 1. In-situ real-time process control pulsed laser deposition system.

interest for its possibilities in manufacturing films. Pulsed laser deposition (PLD) is a method for making very high quality films, and is considered, to be, among the available methods, the best compromise between speed and quality, at least for the foreseeable future. Deposition processes have been used to grow many different metals and semiconductors, including Ag, Al, Cu, Ni, Cd, Cr, Nb, V, Si, GaAs, and their oxides.

This paper deals with two topics illustrating how modeling and computation are aiding the applied scientist in laser materials processing. The first topic deals with the difference in light/matter interaction between metals and oxides, in particular in identifying thresholds for the onset of ablation. Practically all materials can be treated using lasers. However the setting of power parameters is a function of the energy absorbed in the light/material interaction and the thermal properties of the specific material. Thus, there may be a difference of several orders of magnitude of the power settings to accomplish a particular task for different materials. And of course, some lasers will be better matches than others for a particular task on a given material. The actual light energy available to a workpiece depends on the laser power, frequency, optical train, and ambient atmosphere. The energy absorbed depends on the optical properties of the material, the surface finish, and temperature and phase of the material. This energy is converted into heat available for conduction, radiation, and the latent heat of melting and vaporization. A challenge that arises in the numerical modeling is the fact that the thermophysical properties of different classes of materials are highly temperature dependent. It is useful to approach numerical experimentation in a manner analogous to physical experiments, using nondimensional constants that can characterize different regimes of interaction. We have assembled a database of optical and thermophysical properties for metals, alloys, and ceramics. These include Ag, Al, Cu, Ni, Al_2O_3, CuO, NiO, CeO_2, , UO_2, Y_2O_3, ZrO_2, and $YBa_2Cu_3O_7$. We treat both single-crystal transparent dielectrics and "black" phase ceramics. The lasers that we have considered range from the UV (ArF, KrF, XeCl), to VIS (ruby), and IR (Nd:YAG). Although some lasers, such as Nd:YAG and ruby are capable of sustaining power for milliseconds, we restrict attention to pulsed lasers with pulselength in the range 10ns to 100ns. This is taken up in section 2.

The second topic deals with the possibility of temperature control in pulsed laser deposition. The pulsed laser deposition schematic is shown in Figure 1. A pulsed high energy laser beam is used to energize a target in the way which is dealt with in the first section. The energized material leaves the target with high kinetic energy in a supersonic plume, reacts with a background gas, and is deposited on a heated substrate, where the polycrystalline film grows. The target and substrate are mounted in a vacuum chamber wherein the ambient pressure is controlled. There are dozens of process control variables some of which can be adjusted in real-time. These include the laser parameters: laser excitation voltage, optical train focal length, laser repetition rate, laser beam angle of incidence, laser beam footprint; the target controls: target positioning, target motion, beam position on target; the substrate controls: substrate orientation, substrate motion, subsrate temperature; chamber ambient gas pressure; substrate-target distance; applied electromagnetic fields; and total time duration of deposition. Useful output parameters are much more difficult to isolate. The parameters needed to measure the quality of the film are measured ex-situ, and will not be mentioned here. These parameters, both electromagnetic and material, should be correlated with in-situ sensors. This correlation is not perfect and the real-time measurements of in-situ sensors are very difficult to interpret. These include different spectroscopic outputs including emission spectroscopy and laser induced fluorescence, mass spectrometry, Raman spectroscopy, as well as electromagnetic probes and visualization probes. In the future, one should be able to feedback complex information obtained from a combination of sensors. In particular, one should theoretically be able to read many of the relevant properties in real-time at the surface of the growing film using Raman spectroscopy. However, the extreme operating conditions in the PLD rig have limited the practical use of Raman sensors, which would presumably be the most sensitive method of obtaining in-situ information about the deposition process. As presently wired, a typical test-bed feedback control law would consist in, for example, the use of the time-of-flight signal of an ultraviolet emission line from excited copper atoms fed back to the primary control of laser excitation voltage. The difficulty inherent in the automatic feedback proces control of PLD is hinted at by the arrangement. The laser excitation voltage is related to the laser fluence or intensity as deposited on the target, which is an obvious variable to enter physical and mathematical models of the process. However, the relationship is not monotone and is coupled to other variables. At the same time, the time of flight of one spectral emission line gives limited information about the hydrodynamic plume and nothing direct about the deposition process nor indicates how the growth process might be coming along. There are interesting features of the time-of-flight signature, such as double peaking, that are presently the object of intense debate. Our intention in the second part of this paper (section 3) is to demonstrate with theory, experiment, and computation, the strong influence that substrate temperature has on the ablation plume and thus make a strong case for temperature control more generally, in laser ablation process control.

2. Energy flow in laser treatment of materials

The laser pulse lasts between tens of femtoseconds up to hundreds of nanoseconds. During this time, which can be long relative to the times characteristic of the basic interaction, the target material can become multi-phased as the solid melts and is ablated, either evaporatively or explosively. Furthermore, there is

sometimes charge separation as a plasma cloud forms. Thus, there are several competing pathways for the light energy to be converted to other forms. On the shortest time scales, that of the optical excitation of electrons in a metal or of excitation of quasi-particles in a dielectric, one must take into account the disparate relaxation times of the electron system and the lattice-vibrational system of the solid. Thus, we consider two temperatures, T_e, the temperature of the electrons, and T_i, the temperature of the ions in the lattice. The interaction between these thermodynamic systems can be modeled via diffusion equations with a weak coupling between them:

$$C_e(T_e)\frac{\partial T_e}{\partial t} = \frac{\partial}{\partial z}(\frac{T_e}{T_i}k_e\frac{\partial T_e}{\partial z}) - B(T_e - T_i) + Q$$
$$C_i\frac{\partial T_i}{\partial t} = \frac{\partial}{\partial z}(k_i(T_i)\frac{\partial T_i}{\partial z}) + B(T_e - T_i),$$

where Q, the source term, is the laser power absorbed, and z is the coordinate normal to the surface. It is reasonable to assume that the process is one-dimensional on the fast time scales where this model is valid. At later stages (on longer time-scales), the situation may be higher dimensional, but by that point the two thermodynamic systems can be considered to have achieved equilibrium with one another. Higher dimensional models are only really necessary for long pulsed systems or continuous (CW) laser work. The correct scaling depends on the the power absorption; for high power absorption ($\sim$GW cm^{-2}), the two temperature model is necessary in order to model the ablation, but for moderate intensities, where power is delivered over tens of nanoseconds, a single-temperature multi-phase thermal model is sufficient. The material properties, like the optical properties, depend generally on the temperature and may be discontinuous at a phase boundary, so that we have the pair of equations,

$$c_s(T)\rho_s\frac{\partial T_s}{\partial t} = \frac{\partial}{\partial z}(k_s(T)\frac{\partial T_s}{\partial z}) + Q_s \tag{1}$$
$$c_l(T)\rho_l\frac{\partial T_l}{\partial t} = \frac{\partial}{\partial z}(k_l(T)\frac{\partial T_l}{\partial z}) + Q_l, \tag{2}$$

where the subscripts s and l refer to the solid and liquid regions, respectively.[1] These equations are supplemented by the boundary condition,

$$T_s \to T_0, \quad z \to \infty, \tag{3}$$

where T_0 is the controlled heat of the workpiece or target, as well as conditions at the phase interfaces, $z = a_{sl}(t)$, and $z = a_{lv}(t)$. At the solid/liquid interface, conservation of energy requires

$$k_s\frac{\partial T_s}{\partial z} - k_l\frac{\partial T_l}{\partial z} = \rho_s L_m\frac{d}{dt}a_{sl},$$

where L_m is the latent heat of fusion. Superheating has been shown to have thermal effects on the order of several percent for some laser processing applications, however for the nanosecond timescales which are our main focus it is considered negligible and we will ignore it as well as the (Gibbs-Thomson) role of interface curvature. It is a straightforward task to verify the consistency of this assumption. Energy conservation at the liquid/vapor interface gives

$$k_l\frac{\partial T_l}{\partial z} = \rho_l L_v\frac{da_{lv}}{dt},$$

[1]The specific heat here, c, is the specific heat measured under conditions of constant pressure; however, for liquids and solids, $c_p \approx c_v$, so we will ignore this distinction.

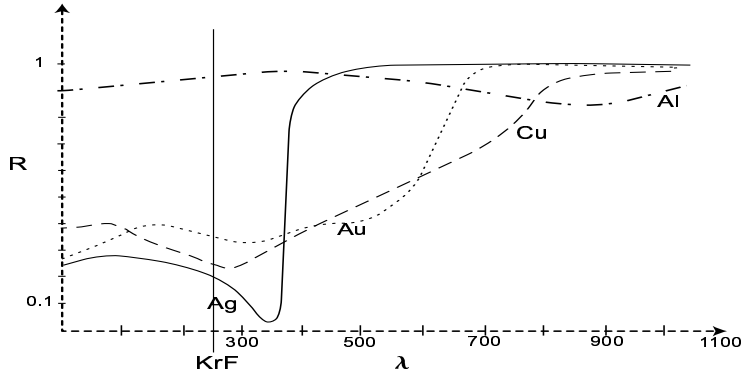

FIGURE 2.

and the kinetics of evaporation mean that

$$\dot{a}_{lv} = \frac{da_{lv}}{dt} = v_* e^{-\Delta h/kT_{lv}},$$

where Δh is enthalpy of vaporization (per molecule), v_* is approximately equal to the speed of sound in the material, and T_{lv} is the temperature at the interface. A result of these relations is the fact that T_{lv} can be much larger than T_v, the normal boiling temperature. This temperature also depends on the vapor saturation pressure. The laser-induced heat flux is given by

$$q = (1 - R(T))e^{-\int_0^z \alpha(T(z'))\,dz'} I(x, y, t),$$

where R is the reflectance, which depends on the photon frequency as well as on the temperature and phase of the material, α is the linear absorbtion coefficient (which also depends on photon frequency and temperature and phase of the material)[2], I is the intensity of light radiation incident on the surface, and z is the distance into the condensed material, normal to the surface. Figure 2 displays the optical wavelength dependence of R for some metals. The heating rate density source term is thus, for constant absorption coefficient,

$$Q = (1 - R)\alpha e^{-\alpha z} I(x, y, t).$$

The laser spot is not symmetric and generally a non-trivial function of the tangential variables, x and y. Although the spatial profile of the excimer-type laser illumination spot is usually taken to be roughly rectangular, it varies with time and, particularly, between shots, in unpredictable ways. It is very difficult to measure irradiance at all, let alone in real time. It will be explained below how, for the timescale of interest, this problem can be considered one-dimensional. The laser pulse intensity will be assumed to have the characteristic excimer form:

$$I(t) = I_0 (\frac{t}{\tau_p})^{\mu} e^{-t/\tau_p},$$

[2]The temperature dependence of α is slight and usually taken to be $\alpha(T) = \alpha_0 - \alpha_1(T - T_{ref})$, where α_1 is several orders smaller than α_0. Because this effect is small compared to other nonlinear effects in this model, we will ignore the temperature dependence of α, except for the change upon melting. In general, $\alpha = (4\pi/\lambda)k'$, where k' is the extinction coefficient (the imaginary part of the complex index of refraction).

rather than the Gaussian pulse that is sometimes used (and characteristic of the older generation of lasers). The relation that τ_p, which we will call "pulse length," has to the full-width half-maximum (FWHM) of pulselength is

$$\tau_p/\tau_F \approx 1.2.$$

There are several approaches to the scaling of the problem. If we take as characteristic time scale for the problem, the pulselength τ_p, and from this form the diffusion length, $l_D = \sqrt{D\tau_p}$, which we take to be the characteristic length scale. The diffusivity, D, is defined to be

$$D = \frac{k_s(T_0)}{c_s(T_0)\rho_s}. \tag{4}$$

If material parameters are assumed to be independent of temperature within each phase, then the equations become:

$$\frac{\partial\theta_i}{\partial\tau} = \frac{\partial^2\theta_i}{\partial\zeta^2} + \Gamma P(\zeta,\tau), \quad i = l, s, \tag{5}$$

where

$$P(\zeta,\tau) = e^{-(\alpha l_D \zeta - a_{lv})}\tau^{\mu} e^{-\tau}. \tag{6}$$

The dimensionless parameter,

$$\Gamma = \frac{\alpha(1 - R(T_m))I_0\tau_p}{c\rho(T_v - T_0)},$$

appears multiplying the source (6). ¿From the form of the equation (5), it follows that the dimensionless number, $\Gamma/\alpha l_D$ is a measure of the ratio of absorbed light energy density to energy density needed to reach the vaporization temperature. Table 1 displays representative values of Γ for various materials. If a number does not appear for an entry it indicates that data was not available or the particular material is transparent for the given laser wavelength. On the other hand, a value of Γ may appear for a wavelength at which pure, single crystals of the material is transparent, in which case data is given for impure samples. For example, optical quality single-crystal saffires and oxides can be transparent (to ultraviolet and visible light), but doped and/or polycrystalline samples can be highly absorbing (black phase). Numerical computations bear out the intuition that Γ is indicative of maximum temperature rise, while $\Gamma/\alpha l_D$ gives a lowest-order prediction of the overall phase change.

The boundary condition (3) becomes

$$\theta \to 0, \quad \zeta \to \infty.$$

At the melt interface, we have

$$\frac{\partial\theta_s}{\partial\zeta} - \beta\frac{\partial\theta_l}{\partial\zeta} = \eta_m\frac{da}{d\tau}$$

where $\beta = k_s/k_l$ is the ratio of the conductivities at the melt temperature, and η_m is a dimensionless constant characterizing the relative size of the enthalpy of fusion compared to the rest of the energy required to reach the boiling temperature (this number, for constant parameter values, is the reciprocal of the Stefan number. Values of β are typically $\approx 2.25 - 2.5$ for metals, ≈ 1 for ceramics.

The simulations based on this model were made by use of the enthalpy method ([3], [4], defining a nondimensional enthalpy of formation. The enthalpy method is particularly suitable for our purposes because it can easily incorporate the nonlinearities due to the temperature dependencies of the material parameters, and,

since we are mainly concerned with the approximate size and evolution of the melt region, we avoid the usual difficulties with front-tracking. The numerical method was implemented using finite-differences. The enthalpy, or heat content per unit volume, is given by

$$H = \int_0^T \rho c(T') + \rho L_m \delta(T' - T_m)\, dT',$$

where the specific heat follows an empirical law,

$$c(T) = a + bT + cT^2 + dT^3 + eT^{-2},$$

where the coefficients are tabulated in various references (e.g., [6],[7]) or else matched to data tables or graphs from other sources (e.g.,[5], [8], [9], [10], [11], [12]). The temperature dependency of the thermal conductivity is taken care by means of the Kirchoff transformation,

$$W = \int_0^T k(s)\, ds.$$

The nonlinear function, $k(T)$, is much harder to match to a general formula in integral powers of the temperature. One is forced to match tabulated data for restricted ranges of temperatures, in this case from $500K$ to the melting temperature. Reported data for the temperature dependence of liquid metals is fairly accurate, but published measurements of the temperature dependence of thermophysical properties for ceramics in the liquid state are known to have uncertainties of as much as 40% ([13], [14], [15]). A weak formulation of the model is then considered using the variable H and W by using an integral operator form of the heat conservation law. It is a straightforward matter to extend usual convergence analysis to the present case under the assumption of a bound on the nonlinear functions. This results in a more restrictive stability condition for the explicit method, and in practice, the time-step is necessarily much smaller than order of square of the space interval. The results presented in the next section were obtained with a time-explicit implementation written in Fortran 90 and executed on a DEC Alpha and a SunSparc Enterprise 3000.

Because of the short optical skin depth of metals, it would be expected that such materials see the laser input as a form of surface heating. This intuition is born out as shown in Figures 3 and 4, which represents the simulation results for a metal with relatively low conductivity (e.g., nickel). The melt region, which has a well-defined interface penetrates into the material a distance on the order of the diffusion length and resolidification starts as soon as the source dies out. The extent in space-time of the melted region depends slightly on the parameter β as indicated by Figure 5.

Figures 6 and 7 portrays the results of a calculation using material parameters typical of a "black" oxide, with optical properties between those of a semi-transparent oxides and metals. A small absorption coefficient and low thermal conductivity combine to ensure that the material "sees" a practically uniform body heating. Physically this should correspond to the establishment of a "mushy" region, as reported in [4] and [16]. The length scale for the graph in Figure 6 is physically within an order less than that displayed in Figure 4, but corresponds to about 50 diffusion lengths. As is seen in Figure 7, the rise to maximum temperature (just above the melting temperature) is fast. The computed "mushy" region is clearly visible and lasts several pulselengths; however, when kinetics of nucleation and interface formation are taken into account, along with the minimal temperature rise over the melting temperature, one expects the physical "mushy" region to be more considerable. The time scale is about 30 pulse lengths (close to 1 μs).

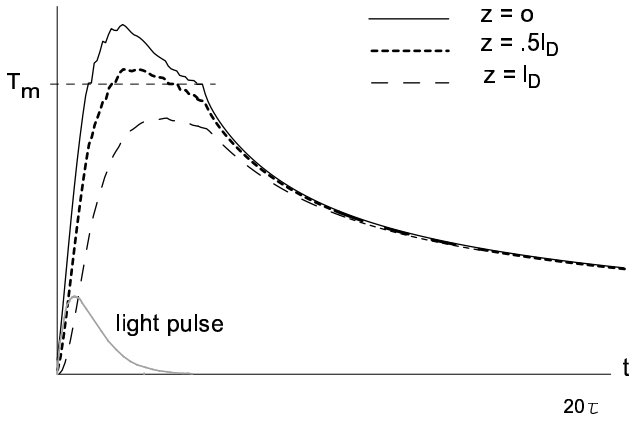

FIGURE 3

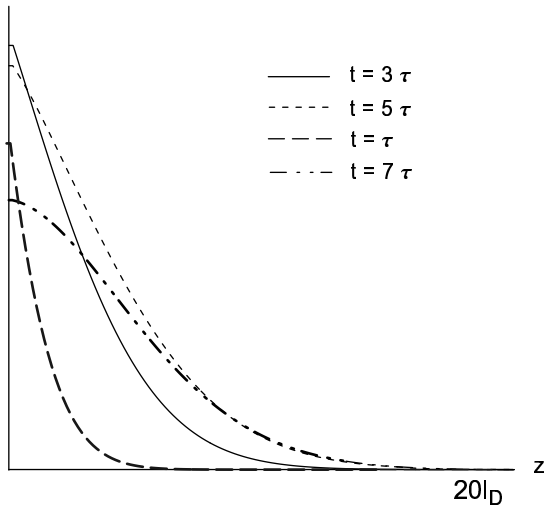

FIGURE 4

Computations with realistic models can give some indication of the thermal effects of laser treatment of particular materials. Furthermore, they can help show us what to expect in other uses, such as ablation or use of a rapid sequence of pulses. For metals, rapid solidification means that for a inter-pulse time period which is long compared to the pulse length, the pulse works on an unheated solid. For oxides, the surface never really cools between pulses and for rapid pulsing may even be liquid up to next pulse. Treating surfaces which are softened may smooth ablative damage, but then there arise concerns with "splashing." Software based on computational models such as this, coupled with databases of large classes of materials, can help the experimentalist and process engineer know what to expect during the material processing, as well as the problem of material choice. Furthermore, as this modeling

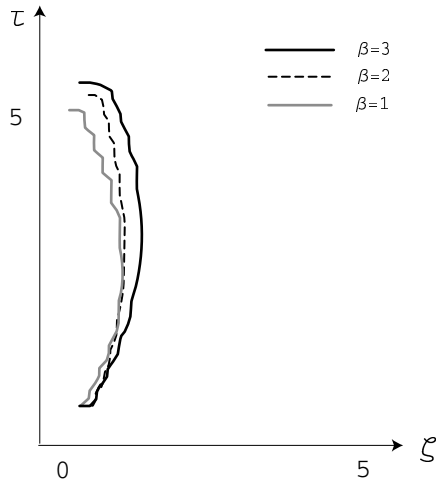

FIGURE 5

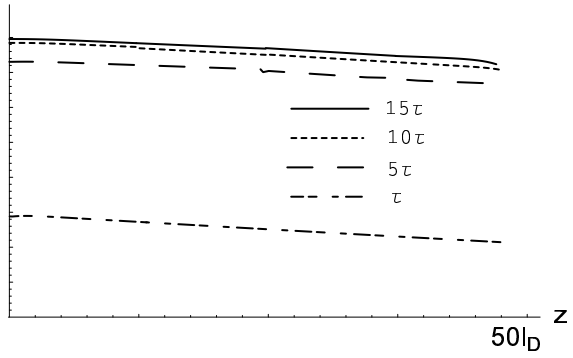

FIGURE 6

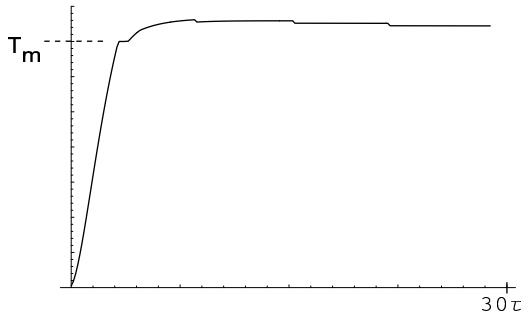

FIGURE 7

becomes more sophisticated and the databases become more detailed, it can be used for the inverse problem of "designing" materials that will behave in a prescribed fashion.

3. Temperature control of pulsed laser ablation

A solid target illuminated by a laser pulse with peak power on the order of 10^8–10^9 W cm^{-2} will produce a plume of ablated particles having energies on the order of 10 eV ejected from the target surface at supersonic velocities. In laser ablation of metallic oxide targets, non-equilibrium vaporization of the target material will result in a multi-component plume. When ablation occurs in vacuum, the plume will tend toward free molecular flow after an initial transient adiabatic expansion. When ablation occurs in the presence of a background gas, the plume structure will include a "snowplowing" shock wave ahead of the ablated material as well as secondary shocks in the plume itself. The gas immediately behind the shock is dissociating and the companion "contact surface" is a reaction zone. A distinctive feature of the ablation plume is the highly transient and relaxing nature of the flow ([20]) . Numerical simulations have exhibited the spatial structure of the shocks as well as vortices and other hydrodynamic features. Laser ablation of non-biological materials is often carried out with the intention of growing films from the target material (making incidental use of possible reaction with the ambient gas). The material to be grown deposits on a substrate a certain distance from the target. Since the plume is highly transient (having a lifetime of several dozen microseconds), real-time flow visualization is limited. Visual spectrum imaging gives only part of the picture and use is made of other available sensors: emission spectroscopy, laser induced fluorescence, mass spectrometry, Raman spectrometry. The appearance of the plume varies according to the spectral window used, and so the use of any particular mode of imaging can be misleading.

Process control parameters include laser pulse energy, deposition time, beam focus, chamber pressure, substrate heater temperature, and pulse repetition rate. As reported in [18], the real-time signature of the ablation plumes have been studied and characterized, including the time-of-flight emission spectroscopy, resolved emission imaging, and fast visible imaging. The ablation plume studies in that report involved oxide systems and, in particular, highlighted the role played by the substrate heater acting on the plume dynamics. When the substrate heater was isolated as an experimental parameter the plume exhibited variation in size and emission intensity similar to the effect of changing the laser beam energy. Moreover, and in contrast, the use of heater as control changed the shape of the plume. Furthermore, varying the substrate temperature had *no discernable effect when ablation was done in vacuum.*

The evidence given by both emission spectrometry and video shows plume shape dependence on substrate temperature. For example, the time-of-flight of copper decreased with increasing substrate temperature, while comparing emissions from sensors at different positions indicated a focusing of the plume at higher temperatures. The emission signal of a plume element such as Cu* and Ba* becomes more complicated as the heater/substrate surface is approached. The signal develops an additional peak, a V_{max2} ([18]). There is no additional peak detected when the heater is removed from the chamber. Visual images associated with higher temperature extended longer along the axis of flight, consistent with the copper emission signal. Extreme "necking" of the plume was quite pronounced in a few cases. Measurements of the cross-section of the image, when fitted to the function,

$\cos^n(\theta)$, where θ is the angle off the longitudinal axis, give $n = 35$–100 or more. This shows that the plume is in fact more forward-peaked than has been indicated by previously reported measurements which were made, not directly on the plume, but indirectly by film thickness measurements. The pictures of a plume, either in vacuum, or in ambient without substrate heating show the usual rounded cosine shape, but when substrate heating is present strong vorticity is generated at the 'wings' of the plume, leading to recirculating flow, greater mixing, and thermalization in those regions, but allowing a more focussed quasi-one-dimensional jet to be produced along the flow axis as the plume nears the substrate heater. The plume observations reported in [18] gave rise to the models and explanations in that paper, in [19], and in this note.

For the purposes of this paper, a simplified model, using flow variables that are averages of the variables corresponding to the components is sufficient to account for some of the observed plume shape evolution, and we need not be concerned with the full chemistry of the plume. At the end of the paper, we will discuss extensions of the model to account for detailed spectroscopic observations.

The flow variables $(\mathbf{u}, \rho, p, T)$ are defined as follows. The species mass conservation takes the form

$$\frac{\partial}{\partial t} n_i + \nabla \cdot (n_i(\mathbf{u} + \mathbf{V}_i)) = g_i, \quad 1 = 1, \ldots, M,$$

where n_i is the species number density, $\mathbf{V}_i$ is the species peculiar velocity, and g_i is the species production or decomposition, for each species i. Summing over all species, we have the bulk mass conservation equation,

$$\frac{\partial}{\partial t} \rho + \nabla \cdot (\rho \mathbf{u}) = 0.$$

The equation of motion for the mixture,

$$\rho \frac{\partial}{\partial t} \mathbf{u} + \rho \mathbf{u} \cdot \nabla \mathbf{u} + \nabla \cdot P = 0, \tag{7}$$

is written in terms of a total pressure tensor. If we assume that relaxation is dominated by collisions, and each fluid "particle" is in local thermodynamic equilibrium, then we can derive equations for the temperatures. The total pressure tensor is written

$$P = \sum P_i,$$

where the pressure for each component is that of an ideal gas,

$$p_i = \rho_i \frac{R}{m_i} T_i.$$

The overall mixture will then satisfy an ideal gas equation of state,

$$p = nRT,$$

if we define a (mixture) temperature as

$$T = \frac{1}{n} \sum n_i T_i,$$

where $n = \sum n_i$, where T_i represents the average kinetic energy of the ith species.

Large-scale numerical computations of the plume were carried out under a wide range of operating variables. The Navier-Stokes equations for one-component and multi-component fluids in two space dimensions were used as the underlying model. For all calculations, the initial field was a steady state fill of O_2 at 150 mTorr with heat delivered to the block 7 cm from the target. A coarse mesh with $\Delta x \sim .5$ cm was used in the outer regions of the computational domain, well away from

the evolving plume; this is gradually refined to $\Delta x \sim .1$ mm in regions of high field gradients. The local mesh refinements were applied at several times in the plume evolution in a manual fashion according to a study of the solution. This was done, typically, every 1μs. Based on the modeling estimates mentioned above, we need about $\Delta t = 10$ ns to resolve the forming plume, and $\Delta t = 50$ ns for the transported and cooling plume. However, a stable and accurate solution was not achieved until Δt was reduced to about 1 ns, and even smaller in some cases. The main features of the plume shape in the presence of substrate heating can be demonstrated with a one-component fluid without relaxation, indeed, as we will see below, viscosity is not needed to produce mixing. The difference between the computed plumes without substrate heating (Figures 8 and 9) differ dramatically from the computed plumes in the presence of a temperature gradient (Figures 10, 11, 12), conforming to the difference that one observes in the actual plume. A comprehensive collection of simulation results, including animations, can be found on the author's web site. One of the prominent features observed in the simulations are relatively large scale vortices at the oblique wings of the plume. Recirculating flow and strong mixing occur there giving rise to collisional processes that result in a strong emission sometimes showing a double peak in the density time-of-flight. The sense of the vortices is what we will refer to as *expected orientation*.

An analytic model explaining this behavior can be derived from the fundamental equations. Using the thermodynamic relation for the specific enthalpy,

$$dh = Tds + \frac{1}{\rho}dp,$$

where s is the specific entropy, we can write the momentum equation (neglecting viscosity) as

$$\frac{\partial \mathbf{u}}{\partial t} - (\mathbf{u} \times \boldsymbol{\omega}) = -\nabla(\frac{1}{2}u^2) + T\nabla s - \nabla h. \tag{8}$$

The equation for vorticity is obtained by taking the curl of the equation of motion to arrive at

$$\frac{\partial \boldsymbol{\omega}}{\partial t} - \nabla \times (\mathbf{u} \times \boldsymbol{\omega}) = \nabla T \times \nabla s. \tag{9}$$

The rate of change of shape of a fluid "particle" is determined by the local rate of strain. which is measured by the vorticity field. It is a necessary component of any shearing motion and any convective deformation giving rise to mixing action on the fluid scale (much larger than mean free path scale). The expression

$$\nabla T \times \nabla s, \tag{10}$$

plays the role of vorticity "source." Certainly a shock can be a source of entropy, but this is not significant for weak shocks. In the reacting plume, entropy is generated as well in the reacting zone behind the compression shock. A curved shock will generate vorticity [22], and an imposed temperature gradient can amplify this vorticity creation, and supply vorticity even in the absence of curvature. Entropy is generated normal to a shock wave, so the expression indicates that vorticity generation will be enhanced for oblique shocks, even in the absence of appreciable curvature. Upon changing the substrate heater from, say, 200C to 550C, mechanical equilibrium is reestablished in about 40 seconds, but it takes less than .1 s to reestablish this equilibrium after a pulsed ablation plume has disturbed it. This (conservative) estimate is based on a quasi-static approach to equilibrium where the steady-state temperature gradient is established while $\nabla p \sim 0$. In this way, the plume (albeit not steady), will always propagate up a one-dimensional temperature

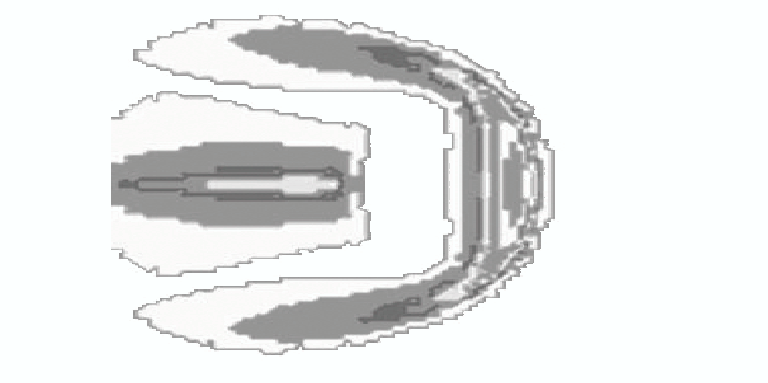

FIGURE 8. Computed shock wave of an ablation plume. Temperature contours are shown.

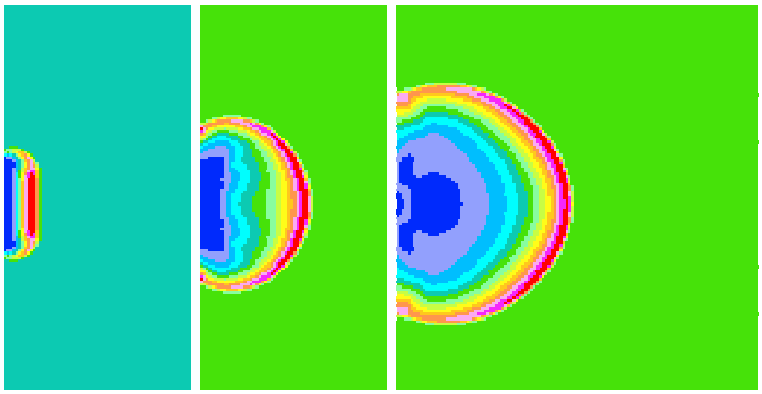

FIGURE 9. Computed shock wave of an ablation plume. As in Figure 8, temperature contours are shown. The operating conditions are different than in that case.

gradient along the axis of the plume.[3] Our assumption of an ideal gas law allows us to consider from here on a background density gradient.

In regions of vorticity generation, either transverse or streamwise, large-scale mixing, through collisional processes, will dissipate the forward-directed kinetic energy of particles through reaction, recombination, or electronic or vibrational de-excitation, which is observed through emission spectrometry. If most of this mixing occurs in the wings of the plume, the effective plume will have the appearance of a one-dimensional jet. We now show that this is the case. Expressions for the vorticity generated at a shock front have been derived by Hayes[22] and others. A special form of this expression will be derived tailored to the needs of this report.

Consider coordinates (ξ_1, ξ_2, n) in a region of the flow domain near a portion of the (smooth) shock. The coordinates (ξ_1, ξ_2) refer to the shock surface and n to the normal, which latter we take to be euclidean distance from the shock surface, so that every point near the front has the representation $\mathbf{R} = \mathbf{r}(\xi_1, \xi_2) + n\mathbf{n}$, where

[3]The plume doesn't have a precise axi-symmetry owing to the asymmetric location of the laser beam and inherent instabilities at higher pressures.

Material	Laser KrF $\lambda = 248$ nm	System Ruby $\lambda = 694$ nm	Nd:YAG $\lambda = 1064$ nm
Al	6.8	23	34
Cu			
Ni	17	33	65
AL_2O_3	.3	–	.15
CeO_2	6.4	–	.06
$YBa_2Cu_3O_7$	5.6	–	–

TABLE 1. Values of Γ for various materials. This parameter is proportional to the pulse fluence (energy per unit area). The fluence for values appearing in this table corresponded to a common total pulse energy of 150 mJ.

Material	β
Ag	2.29
Al	2.29
Cu	2.40
Ni	2.54
UO_2	1.1 – 1.28

TABLE 2. Values of β for various materials.

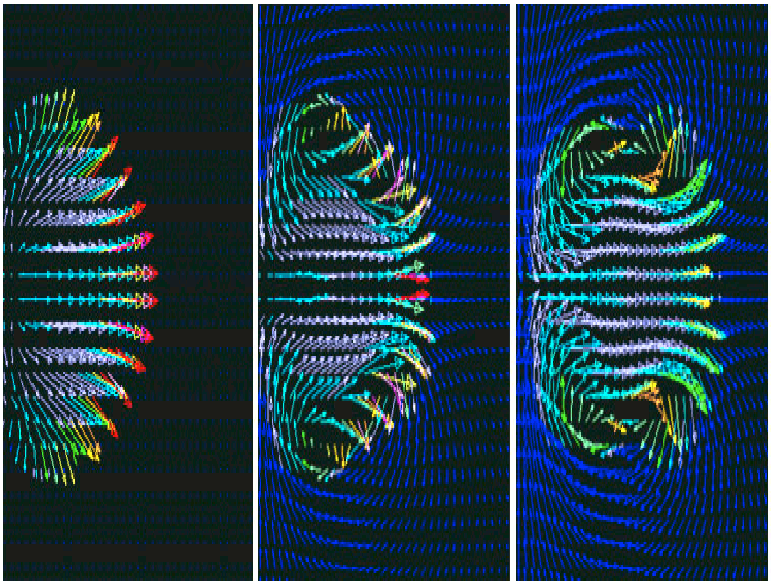

FIGURE 10. Temperature distribution (color) and velocity vectors at three successive snapshots of a plume in an applied temperature gradient, taken about 1 μs apart. It is apparent that in this case a strong recirculating flow is developing.

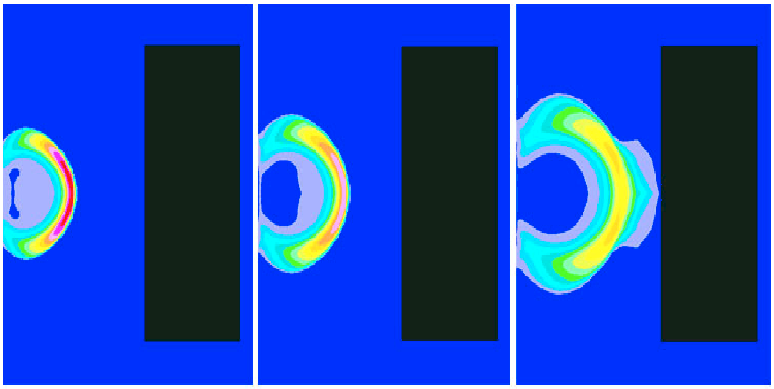

FIGURE 11. Contours of the temperature distribution in the devloping plume, for a set of operating conditions similar to Figure 9 except for the presence of a temperature gradient.

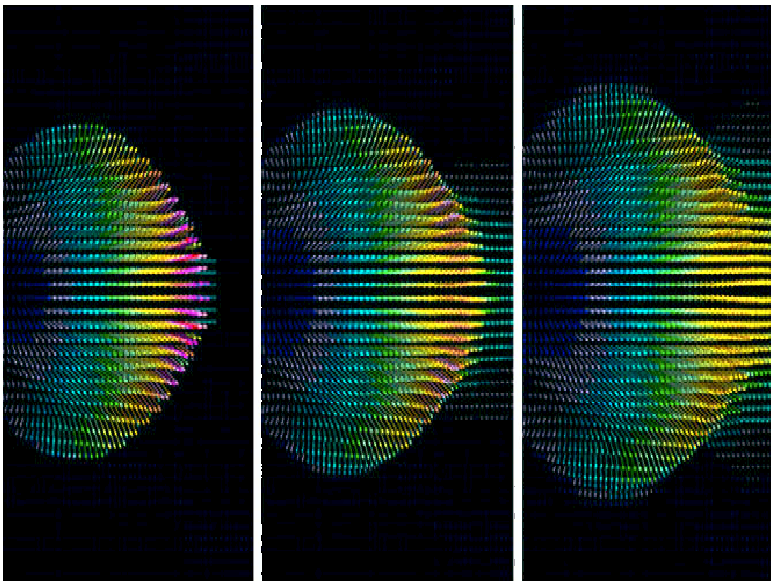

FIGURE 12. Enthalpy (color) and velocity vectors in yet another case. This case corresponds to a greater energy deposition.

$\mathbf{r}$ is the surface parametrization and $\mathbf{n}$ is the unit normal. We use an orthonormal frame in a neighborhood of the shock surface: $\mathbf{t}_1 = \frac{\partial \mathbf{R}}{\partial s_1}, \mathbf{t}_2 = \frac{\partial \mathbf{R}}{\partial s_2}, \mathbf{n} = \mathbf{t}_1 \times \mathbf{t}_2$, where s_k is arclength in the direction of increasing ξ_k: $ds^k = h_k d\xi^k$.

The expression for the vorticity, $\boldsymbol{\omega} = \operatorname{curl} \mathbf{u}$, is, in these coordinates,

$$\boldsymbol{\omega} = (\frac{\partial w}{\partial s_2} - \frac{1}{h_2}\frac{\partial (h_2 v)}{\partial n})\mathbf{t}_1 + (\frac{1}{h_1}\frac{\partial (h_1 u)}{\partial n} - \frac{\partial w}{\partial s_1})\mathbf{t}_2 + (\frac{1}{h_2}\frac{\partial (h_2 v)}{\partial s_1} - \frac{1}{h_1}\frac{\partial (h_1 u)}{\partial s_2})\mathbf{n},$$

and so

$$\mathbf{n} \times \boldsymbol{\omega} = (\frac{\partial w}{\partial s_2} - \frac{1}{h_2}\frac{\partial h_2 v}{\partial n})\mathbf{t}_2 + (\frac{\partial w}{\partial s_1} - \frac{1}{h_1}\frac{\partial h_1 u}{\partial n})\mathbf{t}_1.$$

Using an obvious shorthand, in a special coordinate system where $\mathbf{n}$ is a gradient,

$$\begin{aligned}\mathbf{u} &= u_n\mathbf{n} + \mathbf{u}_{tan} \\ &= (\mathbf{u}\cdot\mathbf{n})\mathbf{n} + \mathbf{n}\times(\mathbf{u}\times\mathbf{n}),\end{aligned}$$

we get immediately

$$(\nabla\times\mathbf{u}_{tan})\times\mathbf{n} = \mathbf{n}\cdot\nabla\mathbf{u}_{tan} + \mathbf{u}_{tan}\cdot\nabla\mathbf{n} = \nabla_n\mathbf{u}_{tan} - \mathbf{S}(\mathbf{u}_{tan}),$$

where $\mathbf{S}$ is the shape operator from surface theory ([21]).

The tangential component of vorticity is

$$\boldsymbol{\omega}_{tan} = \mathbf{n}\times(\boldsymbol{\omega}\times\mathbf{n}) \tag{11}$$

$$= \mathbf{n}\times(\nabla u_n\times\mathbf{n} - \mathbf{n}\times(\nabla\times\mathbf{u}_{tan})_{tan}) \tag{12}$$

$$= \mathbf{n}\times(\mathbf{n}\cdot\nabla\mathbf{u}_{tan} + \mathbf{u}_{tan}\cdot\nabla\mathbf{n} - \nabla_{tan}u_n) \tag{13}$$

$$= \mathbf{n}\times(\mathbf{n}\cdot\nabla\mathbf{u}_{tan} - \nabla_{tan}u_n + \mathbf{S}(\mathbf{u}_{tan})); \tag{14}$$

we also need

$$\begin{aligned}\mathbf{u}\cdot\nabla\mathbf{u} &= \mathbf{u}\cdot\nabla(\mathbf{n}\times(\mathbf{u}\times\mathbf{n}) + (\mathbf{n}\cdot\mathbf{u})\mathbf{n}) \\ &= \mathbf{u}\cdot\nabla\mathbf{u}_{tan} - u_n\mathbf{S}(\mathbf{u}_{tan}) + (\mathbf{u}\cdot\nabla u_n)\mathbf{n} \\ &= \mathbf{u}_{tan}\cdot\nabla_{tan}\mathbf{u}_{tan} + u_n\mathbf{n}\cdot\nabla_{tan}\mathbf{u}_{tan} + \mathbf{u}_{tan}\cdot\mathbf{n}(\mathbf{n}\cdot\nabla\mathbf{u}_{tan}) \\ &\quad + u_n(\mathbf{n}\cdot\nabla\mathbf{u}_{tan}) - u_n\mathbf{S}(\mathbf{u}_{tan}) + (\mathbf{u}\cdot\nabla u_n)\mathbf{n};\end{aligned}$$

where $\nabla_{tan} = \nabla - \nabla_n = \nabla - \mathbf{n}\frac{\partial}{\partial n}$ ([21]).

Jump conditions on the shock surface follow in the usual way from conservation laws or using (14):

$$[\,\mathbf{u}_{tan}\,] = \mathbf{0},$$

$$[\,\boldsymbol{\omega}\cdot\mathbf{n}\,] = 0,$$

$$[\![\,\boldsymbol{\omega}_{tan}\,]\!] = \mathbf{n}\times[\![\,\frac{\partial}{\partial n}\mathbf{u}_{tan} - \nabla_{tan}u_n\,]\!]. \tag{15}$$

The *jump operator*, $[\![\,\cdot\,]\!]$, is the flow quantity behind the shock minus the flow quantity in front of the shock. Since the shock is not assumed to be inertial with respect to the laboratory, we will define a moving coordinate system based on moving the frame introduced above. That is,

$$\mathbf{R}(s_1, s_2, n, t) = s_1\mathbf{t}_1(t) + s_2\mathbf{t}_2(t) + n\mathbf{n}(t).$$

For each combination of (s_1, s_2, n), consider the "flow" of a point following the shock, $t\to\boldsymbol{\Phi}(t)$, then

$$\dot{\boldsymbol{\Phi}} = (\frac{\partial\mathbf{R}}{\partial t})_{s_1,s_2,n} = -\mathbf{V},$$

defines the shock velocity. In analogy, to we also use the notation, $\mathbf{V} = V_n\mathbf{n} + \mathbf{V}_{tan}$, for consistency. Then the normal component of mass conservation gives

$$[\![\,\rho(u_n - V_n)\,]\!] = 0. \tag{16}$$

Let us use the notation $m_s = \rho(u_n - V_n)$ for the mass flux across the shock. Momentum conservation across the shock gives:

$$(m_s)[\![\,u_n\,]\!] = -[\,p\,]. \tag{17}$$

We now differentiate the jump relation (17) along the surface (i.e., apply ∇_{tan}), to get

$$\nabla_{tan}(m_s)[\![\, u_n \,]\!] + m_s [\![\, \nabla_{tan} u_n \,]\!] = -[\![\, \nabla_{tan} p \,]\!]. \tag{18}$$

Meanwhile, the equation of motion, projected onto the surface tangent is

$$\begin{aligned} -\nabla_{tan} p &= \rho((\frac{\partial \mathbf{u}}{\partial t})_{s_1,s_2,n} + (\mathbf{u}-\mathbf{V})\cdot\mathbf{u})_{tan} \qquad (19)\\ &= \rho(\frac{\partial \mathbf{u}_{tan}}{\partial t})_{s_1,s_2,n} + \rho u_n (\frac{\partial \mathbf{n}}{\partial t})_{s_1,s_2,n} \\ &\quad - \rho u_n \mathbf{S}(\mathbf{u}_{tan} - \mathbf{V}_{tan}) \\ &\quad + m_s \frac{\partial}{\partial n}\mathbf{u}_{tan} + (\mathbf{u}_{tan} - \mathbf{V}_{tan})\nabla_{tan}\mathbf{u}_{tan}. \qquad (20) \end{aligned}$$

Now, calculating the difference in the momentum equation (7) on either side of the front, eliminate $[\![\, p \,]\!]$ from these two equations.

$$[\![\, \boldsymbol{\omega}_{tan} \,]\!] = \mathbf{n} \times \left([\![\, \frac{1}{\rho} \,]\!] \nabla_{tan}(m_s) + [\![\, \rho \,]\!] (\frac{V_n}{m_s})(\mathbf{S}(\mathbf{u}_{tan} - \mathbf{V}_{tan}) - \dot{\mathbf{n}}) \right), \tag{21}$$

where we have only included terms that are consistent with the assumption that the shock moves into quiescent gas.

It is the first term in the above expression that involves the thermal gradient in the quiescent gas. The other term, involving the jump in density, is made up of two terms, the first is related to the curvature of the shock front, and the second involves the local rotation of the shock. In order to estimate the relative importance of these terms an analytic expression for the thermal field in the quiescent gas will be used. We can approximate the heated substrate by a flat disk, radius a, held at a fixed temperature, T_s, and, given the geometry, sizes, and materials involved, the temperature at infinity can be taken to be room temperature, T_R. Using the nondimensionalization, $\theta = \frac{T-T_R}{T_R}$, and

$$\frac{\rho}{\rho_{ref}} = \frac{1}{1+\theta} = \frac{1}{1+\theta_s \operatorname{arccot}(\frac{z}{a\cos\theta})}, \tag{22}$$

where θ_s is a nondimensional parameter of order approximately unity when the substrate temperature is in the range

$$T_R < T_s < 4T_R,$$

which is essentially the experimentally considered range. It is reasonable to assume that the density behind the shock is constant. ¿From the functional form of (22) it is seen that there are essentially two regimes: for distances from the target on the order of a, the term $[\![\, \frac{1}{\rho} \,]\!]$ is at least an order bigger than $[\![\, \rho \,]\!]$. Let us examine this expression locally. Assume a planar shock, oriented parallel to the $\mathbf{i}$ axis where the $\mathbf{k}$ axis is perpendicular to the substrate pointing at the target, with $\mathbf{V} = -V(t)\mathbf{k}$, and $\mathbf{n} = -\cos\theta\mathbf{k} + \sin\theta\mathbf{j} = \sin\psi\mathbf{k} + \cos\psi\mathbf{j}$. (Here, ψ is the complement of θ.) This θ is a local parameter, but can be associated with the global variable, θ, for a shock that is approximately spherical. (By choosing this form for the tangent plane, we are assuming an axi-symmetric plume.) In the same way, we will use the variable, z, which can be replaced by $\frac{z}{a\cos\theta}$ in a global treatment. The mass flux is $m_s = \rho\sin\psi V$, and

$$\nabla_{tan}(m) = -\cos\psi\sin\psi V\frac{\partial\rho}{\partial z}. \tag{23}$$

Since $[\![\frac{1}{\rho}]\!]$ is negative, the vorticity produced is of the *expected orientation*. Furthermore, in the early regime, before the plume decelerates and while that factor is large, the term (23) is small along the longitudinal axis of the plume and only is significant off-axis. Now let us examine the rotation term, using the same local plane. Here, $\dot{\mathbf{n}} = \mathbf{\Omega} \times \mathbf{n}$. First, consider the rotation towards or away from the substrate, i.e., $\mathbf{\Omega} = \omega \mathbf{i}$, with $\omega < 0$ or $\omega > 0$, respectively. This gives rise to a transverse vorticity production term,

$$-\omega(\frac{V_n}{m})[\![\rho]\!]\mathbf{i}.$$

Furthermore, this term is opposite signed to that which would be produced due to the curvature. An arbitrary rotation can produce streamwise vorticity as well; let $\mathbf{\Omega} = \omega_x \mathbf{i} + \omega_y \mathbf{j} + \omega_z \mathbf{k}$, then the corresponding vorticity production term is

$$[\![\rho]\!](\frac{V_n}{m})\left(-\omega_x \mathbf{i} + (\omega_z \cos\psi - \omega_y \sin\psi)\mathbf{X}\right),$$

where $\mathbf{X}$ is a unit vector along the tangent plane, perpendicular to $\mathbf{i}$. Note that streamwise vorticity production can be zero even in the presence of rotation.

In this way, we have identified a hydrodynamic mechanism operating in the plume that can, at least partly, account for the plume shape changes and the "necking" that is observed in both emission spectrometry and fast visual imaging experiments. Significant increase in signal intensity with increasing heater temperature as monitored at the same viewing position, was seen in the excited Cu (Cu*) emissions from both the CuO and YBCO targets. Fast visual imaging shows necking and jet-like features. Two dimensional plume dynamics simulations accounting for most of the multi-physics shows these effects quite clearly. The substrate temperature can be as powerful a process parameter as gas pressure and/or laser energy.

4. Discussion

We have have ignored reaction kinetics in the plume and the target material, and there are prominent experimental anomalies that cannot be explained using a single-component non-reacting flow. For example, in the experiments dealing with substrate temperature, variations in TOFs with gas species type are more complicated in the different trends measured at 327nm and at 520nm. The TOF of the 327nm component is identical at the midway position in both O_2 and Ar . However this changes near the heater where the Cu* component is slower in O_2. This trend is reversed with the 520nm Cu* component in Ar. Here the TOF is less in Ar at the midway position but equal near the heater. The TOF of the 553nm Ba* component from a YBCO target, behaves similarly to that of the Cu* from the CuO target. The TOF as measured at a midway position decreases with increasing heater temperature. In addition, the development of multiple peaks in the emission signal near the heater surface indicates an increase in plume dynamics complexity at the position where the film is grown. Controlling the TOF of one or more emitting plume components at the multiple peak position might enable increased process control. (When the plume is in this region, molecular dissipation, neglected in the analysis given above, is expected to come into play.) The amplitude difference between the two peak amplitudes is expected to be very sensitive to small changes in the control input (laser excitation voltage). This would be process control based on very small easily monitored emissions from the region where the film is actually growing.

References

[1] J. F. Ready, Effects of high-power laser radiation, Academic Press, 1971

[2] A. M. Prokhorov, V. I. Konov, I. Ursu and I. N. Mihailescu, Laser heating of metals, Adam Hilger, 1990

[3] J. Crank, Free and moving boundary problems, Clarendon, 1984

[4] D. R. Atthey, A finite difference scheme for melting problems, J. Inst. Maths. Applics. 13 (1974) 353-356

[5] Armour Research Foundation, Handbook of thermophysical properties of solid materials, Macmillan, 1961

[6] E. A. Brandes and G. B. Brook, Smithell's Metal Reference Book, 7th Ed., Butterworth and Heinemann, 1992

[7] W.G. Mallard and P.J. Linstrom, Eds., NIST Chemistry WebBook, NIST Standard Reference Database Number 69, February 2000, National Institute of Standards and Technology, Gaithersburg MD, 20899 (http://webbook.nist.gov).

[8] J. O'M. Bockris, J. L. White and J. D. Mackenzie, Physicochemical measurements at high temperature, Butterworth, 1959

[9] N. P. Cheremisinoff, Handbook of ceramics and composites, M. Dekker, 1990

[10] J. R. Davis & Assoc., Aluminum and aluminum alloys, ASM, 1993

[11] D. R. Lide, Handbook of Chemistry and Physics, CRC, 1992

[12] Y. S. Touloukian and E. H. Buyco, Specific Heat – Nonmetallic Solids, Thermophysical properties of matter, vol.5, IFI/Plenum, 1970

[13] H. A. Tasman, D. Pel, J. Richter, and H. E. Schmidt, Measurement of the Thermal Conductivity of Liquid UO2, High Temp.-High Pressures 15, (1983) 419-431

[14] Y. S. Touloukian, R. W. Powell, C. Y. Ho and P. G. Klemens , Thermal Conductivity – Metallic Elements and Alloys, Thermophysical properties of matter, vol.1, IFI/Plenum, 1970

[15] Y. S. Touloukian, R. W. Powell, C. Y. Ho and P. G. Klemens, Thermal Conductivity – Nonmetallic Solids, Thermophysical properties of matter, vol.2, IFI/Plenum, 1970

[16] A. B. Crowley and J. R. Ockendon, A Stefan problem with a non-monotone boundary, J. Inst. Maths. Applics. 20 (1977) 269-281

[17] American Institute of Physics (AIP) Handbook, 2nd Ed., McGraw-Hill, 1963

[18] T. P. Svobodny and R. Biggers, Pulsed-laser ablation plume dynamics: characterization and modeling, High-Power Laser Ablation IV (Ed: Claude R. Phipps), pp.81-92, 2002

[19] T. P. Svobodny and R. Biggers, Ablation Plume Shock Wave in a Temperature Gradient, AIAA-2005-313, 2005

[20] E. W. Kreutz and J. Gottman, Dynamics in Pulsed Laser Deposition of Ceramics: Experimental, Theoretical and Numerical Studies, physica status solidi, 166, 569-580, 1998

[21] T.Svobodny, Shape optimization and control of separating flow in hydrodynamics, in Flow Control, Edited by M. D. Gunzburger, 1995

[22] W. D. Hayes, The vorticity jump across a gasdynamic discontinuity, J. Fluid Mechanics, 2, 1957

Department of Mathematics and Statistics, Wright State University, Dayton, OH 45435

E-mail: thomas.svobodny@wright.edu

URL: http://www.math.wright.edu/MS/AppliedMath/PLD/main.html